Water-Splitting Artificial Leaf Based on a Triple-Junction Silicon Solar Cell: One-Step Fabrication through Photoinduced Deposition of Catalysts and Electrochemical Operando Monitoring

Duc N. Nguyen, Mariam Fadel, Pascale Chenevier, Vincent Artero, Phong D. Tran

Water-splitting artificial leaf based on a triple junction silicon solar cell: one-step fabrication through photo-induced deposition of catalysts and electrochemical operando monitoring

Duc N. Nguyen,[a,b] Mariam Fadel,[b] Pascale Chenevier,[c] Vincent Artero,[b*] Phong D. Tran[a*]

[a] University of Science and Technology of Hanoi, Vietnam Academy of Science and Technology, 18 Hoang Quoc Viet, Hanoi, 100000, Vietnam.

[b] Univ. Grenoble Alpes, CNRS, CEA; IRIG ; Laboratoire de Chimie et Biologie des Métaux; 17 rue des Martyrs, Grenoble 38000, France.

[c] Univ. Grenoble Alpes, CNRS, CEA, IRIG; SyMMES, 17 rue des Martyrs, Grenoble 38000, France

Abstract

Solar hydrogen generation via water splitting using a monolithic photoelectrochemical cell, also called artificial leaf, could be a powerful technology to accelerate the transition from fossil to sustainable energy sources. Identification of scalable methods for fabrication of monolithic devices as well as gaining insights into their operating mode to identify solutions to improve performance and stability represent great challenges. Herein, we report on the one-step fabrication of a CoWO|ITO|3jn-a-Si|Steel|CoWS monolithic device via the simple photo-induced deposition of CoWO and CoWS as OER and HER catalyst layers, respectively, onto an illuminated ITO|3jn-a-Si|Steel solar cell using a single deposition bath containing the $[Co(WS_4)_2]^{2-}$ complex. In a pH 7 phosphate buffer solution, the best device achieved a solar to hydrogen conversion yield of 1.9%. Evolution of the catalyst layers and that of the 3jn-a-Si light

harvesting core during the operation of the monolithic device is examined by conventional tools like SEM, EDX, ICP-OES together with a bipotentiostat measurement. We demonstrate that the device performance degrades due to the partial dissolution of catalyst. Still, this degradation is healable by simply adding $[Co(WS_4)_2]^{2-}$ to the operating solution. However, modifications on the protecting ITO layer are shown to initiate irreversible degradation of the 3jn-a-Si light harvesting core resulting in a 10-fold decrease of the performances of the monolithic device.

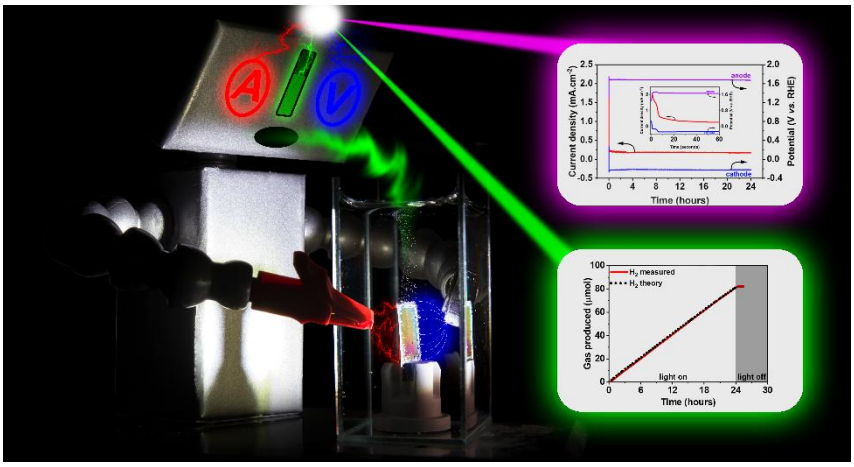

Main Text

Introduction

Solar water splitting represents a potential technological solution for the large-scale production of H_2 fuel in the future. Great efforts are being devoted to develop efficient components, namely hydrogen evolving catalysts, oxygen evolving catalysts and light harvesters, which are required to construct solar water splitting devices. Important progresses have been achieved in the last decade in assembling these components to make bias-free operational devices.[1-4] The first solution relies on metal oxide photocatalysts like $SrTiO_3$, which usually have large band gap and therefore harvest only UV or near UV photons of the solar spectrum. As a result, these photocatalysts offer low solar to H_2 conversion yield (η_{STH}), *e.g.* of ca. 1%.[5-6] However, they are

cost effective, (photo)chemically stable, *e.g.* against the chemical corrosion and are appropriate for integrating within a large-sized device. Domen and coll. demonstrated the safe operation of a 100 m^2 solar farm based on 625 cm^2 photocatalytic sheets obtained by drop-casting $SrTiO_3$:Al nanoparticles on a glass substrate. The system showed a η_{STH} of 0.76% under the natural sun light.[7] Such metal oxides can also be used as photoelectrode materials in tandem photoelectrochemical cells (PEC), sometimes after dye-sensitization and proper combination with catalysts.[8-9] Low band-gap semiconductors such as silicon, III-V materials or organic semi-conductors can also be exploited to prepare PEC prototypes. The second solution consists of using an appropriate solar cell to power a water electrolysis system in a decoupled (wired) configuration. This approach provided the most important progress in the field in term of η_{STH} performance.[5, 10-12] Jaramillo and coll. reported on the use of a InGaP| GaAs| GaInNAs(Sb) triple-junction solar cell to power a dual proton exchange membrane water electrolyser made of Pt/C and Ir/C water electrolysis catalysts.[5] The wired device showed a remarkable η_{STH} of ~30%. Highly efficient photoabsorbers such as silicon,[13-14] III-V semi-conductor junctions,[2, 5] or hybrid organic-inorganic perovskites[10] or their tandem combination[11] were also used. These materials are known to be unstable in the presence of aqueous electrolytes, so that a decoupled configuration, in which the solar cell stays in the air to minimize corrosion while only the two water electrolysis catalyst electrodes are in contact with the electrolyte solution is usually preferred. Despite being efficient and based on two existing mature technologies, such wired solar cell + electrolysis systems involves high capital expenditures that may prevent their adoption by the market for decentralized hydrogen production.[14] An operational wireless device combining the solar cell and the two catalytic electrodes in a monolithic architecture would represent a more practical solution.[1] Such a configuration requires burying the photoabsorbers

within the architecture to avoid contact with the aqueous electrolyte and prevent their corrosion. Following the initial demonstrations by Miller and Rocheleau (Table S1),[15] Nocera and coll. reported on the creation of an artificial leaf based on a triple junction amorphous Si solar cell (3jn-a-Si) coated with a NiMoZn alloy H_2-evolving catalyst and a CoPi O_2-evolving catalyst.[16-18] This wireless monolithic device displays a η_{STH} of 2.5% when being conditioned for operation in a pH 9.2 borate buffer. While this 2011 report revived the field of monolithic devices, limited data are available regarding the actual limitations in terms of light harvesting, catalysis and interface thereof within the system.[1 19-20] In terms of scaling–up the fabrication of the devices to deploy the technology, another limitation comes from the multistep assembly of the device, which requires a photo-assisted electrodeposition of the CoPi catalyst on the anode-side followed by an electrodeposition of the NiMoZn catalyst on the cathode-side of the 3jn-a-Si solar cell.

Over years of intensive development, several promising H_2-evolving and O_2-evolving catalysts made of earth-abundant-elements are available. Among those, bimetallic sulfides like cobalt molybdenum sulfide[19-21] or cobalt tungsten sulfide[22-23] are promising noble metal free H_2-evolving catalysts whereas their oxide/hydroxide counterparts are active O_2-evolving catalysts.[24-27] Even, few of these bimetal sulfides or oxides were reported to be efficient bifunctional or Janus catalysts for driving the overall water splitting.[28-29] These materials can be prepared as thin films on a conducting or a semiconducting electrode *via* electrochemical or photo-assisted electrochemical deposition. For example, some of us reported that, using a solution of $[Co(WS_4)_2]^{2-}$ in a pH 7 phosphate buffer, a cobalt tungsten sulfide layer (denoted hereafter as CoWS) active for the H_2-evolution can be grown at an onset cathodic potential of ~+0.1V vs. RHE (here and after, we arbitrarily define onset (over)potentials as the (over)potential values at which the modulus of the current density exceeds 0.1 $mA.cm^{-2}$).[22] From the same solution, a

cobalt tungsten oxide layer (denoted hereafter as CoWO) being active for the O_2-evolution can be obtained at an onset anodic potential of ~1.3V vs. RHE[24] (*see also* **figure S1**). In a pH 7 phosphate buffer these catalysts operate with respective onset overpotentials of –0.15 V and +1.52 V *vs.* RHE for the H_2 evolution and O_2 evolution processes (**figure S2**). Therefore, a voltage of 1.7 V is sufficient to drive the overall water splitting with CoWS and CoWO catalysts electrodeposited from the same $[Co(WS_4)_2]^{2-}$ precursor.

Herein we demonstrate that a triple junction amorphous silicon (3jn-a-Si) solar cell that offers an open-circuit photovoltage of 1.95V is appropriate to (i) drive the deposition of CoWS and CoWO catalysts, and (ii) subsequently drive the overall solar water splitting with these two catalyst layers. The best monolithic wireless device shows a η_{STH} of 1.9% while working in a pH 7 phosphate buffer electrolyte under the simulated sunlight. We also report how such devices can be instrumented to get additional operando insights regarding the operating potential, photocurrents and the stability of individual components.

Results and discussion

The commercial 3jn-aSi solar cell is composed of three amorphous Si junctions where each junction consists of an intrinsic Si (i: a-Si) layer sandwiched by a p-type (p: µc-Si) layer and a n-type (n: a-Si) layer. The front-side of the solar cell is protected by an indium-doped tin oxide (ITO) layer. The whole solar cell stands on a stainless steel substrate (**figure S3**). Hereafter, we denote the solar cell as ITO | 3jn-a-Si | Steel. For manipulation, it was first cut in small species of 15 ×17 mm^2. The cell edge was then carefully cleaned with a 1M HCl solution to remove any broken Si part that might have negative impact onto the cell operation. The cell edge was then covered by an epoxy resin or just a commercial steel paint. The working area on both the ITO front-side and the Steel back-side was limited to 10×10 mm^2 (**figures S4, S5**. *See SI for detailed*

preparation of the cell). We employed a two-electrode configuration to verify the actual photovoltage that was generated when the cell was illuminated with simulated sunlight (100 $mW.cm^{-2}$; Xe lamp filtered with AM 1.5G filter) in air without being immersed in any electrolyte solution (*see SI for details*). A stable photovoltage of 1.95 V was recorded (**figure 1a,** *inset showing the evolution of photovoltage recorded using the chopped light mode)* which was lower than the value of 2.2 V expected from the product specifications.[30] This observation was confirmed through the V_{oc} of 2.02 V obtained through the characteristic current-voltage plot. The fill factor was recorded at 34.6%, also lower than the expected 67.2% (**figure 1b**), reflecting the lower performances of large commercial samples (here 30 ×20 cm^2) compared to small lab-scale samples.

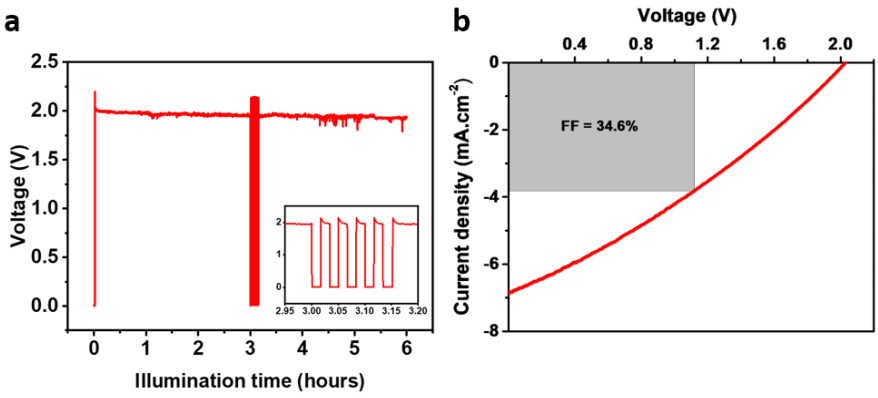

Figure 1. (**a**) Photovoltage generated over time (*Inset shows the evolution of voltage generated under chopping light*); (**b**) I-V curve recorded for a ITO|3jn-a-Si|Steel solar cell under illumination by employing a conventional solar cell configuration. Illumination: 100 $mW.cm^{-2}$ (1 sun) Xe- lamp illumination with AM 1.5G filter.

One-pot fabrication of monolithic device via photo-induced deposition of water splitting catalysts

The ITO | 3jn-a-Si | Steel solar cell was immersed into a pH 7 phosphate buffer deposition bath added with 0.5 mM $[Co(WS_4)_2]^{2-}$ in the aim to grow the CoWO and CoWS catalysts onto the ITO front-side and steel back-side of the solar cell, respectively (**figure 2a**). Upon irradiating the ITO front-side by simulated sunlight, bubbles appeared on both the ITO front-side and the steel back-side, suggesting the occurrence of solar-driven water splitting. The generation of H_2 and O_2 was confirmed by gas chromatography measurements (**figures 2b,c**, black and red traces). In a control experiment using the identical phosphate buffer solution being free of $[Co(WS_4)_2]^{2-}$ precursor, negligible H_2 and O_2 amounts were detected (**figures 2b,c**, green and blue traces), clearly evidencing the role of deposited CoWO and CoWS catalysts in catalyzing water splitting.

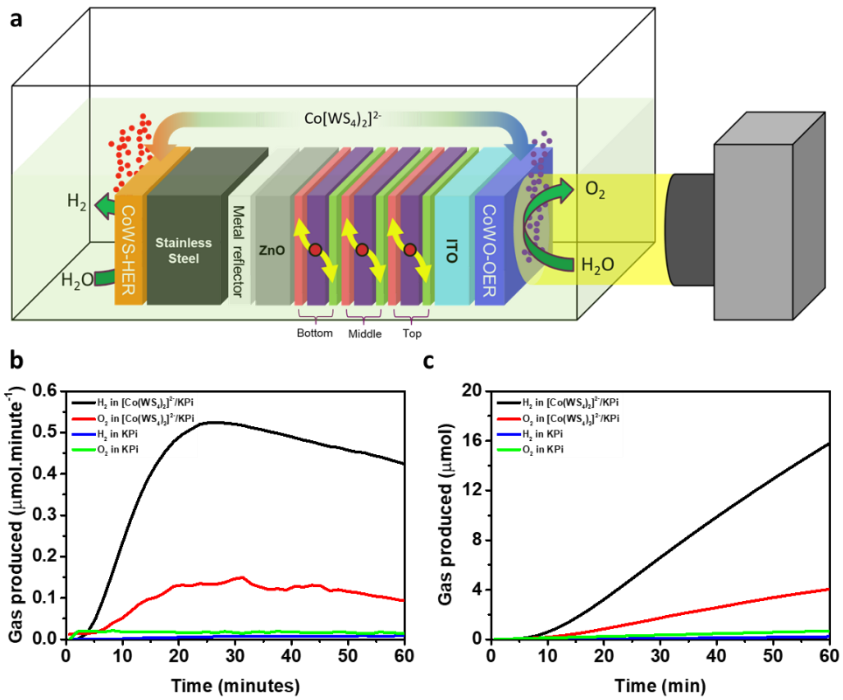

Figure 2. (**a**) Schematic representation of the catalysts assembling process; (**b**) real-time and (**c**) - accumulated amount of H_2 and O_2 gases produced during the assemblage of CoWO | ITO | 3jn-a-Si | Steel | CoWS monolithic device

However, the H_2/O_2 molar ratio was found to range between 4 : 1 and 6 : 1, thus much higher than the expected 2 : 1 molar ratio for overall water splitting. This result suggests that electrodeposition of the CoWO catalyst continues to compete with O_2 evolution to a greater extent than the corresponding reductive processes. In the online gas chromatography analysis, we observed the maximal rate of H_2 evolution after ~20 minutes of operation. However, this value is convoluted with the few-minutes time lag between actual gas evolution on the device and its quantification in the gas chromatograph. We thus conducted an optimization of catalyst deposition time between 1 to 20 min. After catalyst deposition, the resultant monolithic device was taken out, intensively washed with DI water and then naturally dried in air. The resulting monolithic devices were again tested for H_2 evolution in a pH 7 phosphate buffer solution being free of $[Co(WS_4)_2]^{2-}$ (**Table 1** and **figure S6)**. Formation of bubbles during photoelectrochemical water splitting may affect the performance of the device through an increase of the back-scattering losses, thereby decreasing the photocurrent density generated.[31] Noteworthy, the electrolyte was continuously bubbled in our setup with Ar as the carrier gas used for gas chromatographic detection. The resulting convection of the electrolyte was continuously detaching H_2 and O_2 bubbles, potentially adhering to the catalytic layers, therefore limiting this back-scattering effect and allowing to reach a steady state in terms of performances.

The H_2 evolution rate was found to increase with the catalyst deposition time until the latter reached 10 minutes (**Table 1**, entries 1-4). A marginal improvement was found when the time was increased to 20 min (**Table 1**, entry 5) and, in that case, we sometimes observed the detachment of the CoWO catalyst layer from the ITO surface. Thus, we decided to set the catalyst deposition time for 10 minutes for the fabrication of all devices.

We then optimized the chemical composition of the catalyst deposition bath in order to achieve the best monolithic device. Actually, *in situ* formation of the $[Co(WS_4)_2]^{2-}$ species is expected regardless the Co^{2+}/ $[WS_4]^{2-}$ molar ratio employed.[32] However, varying this ratio adds up the excess Co^{2+} or $[WS_4]^{2-}$, which could alter the deposited catalyst performance. Using a 1 mM $[WS_4]^{2-}$ deposition bath free of Co^{2+} did not result in any deposit on the ITO│3jn-a-Si│Steel solar cell. The resultant device showed a negligible performance (**Table 1**, entry 10). A device showing η_{STH} of 1% was obtained when using a deposition bath composed of 0.5 mM Co^{2+} (no $[WS_4]^{2-}$; **Table 1**, entry 9). In this case, deposition of a cobalt-oxide-based O_2 evolution catalyst (*e.g.* CoPi having onset deposition potential of +1.1V vs. NHE[33]) and a cobalt-based H_2 evolution catalyst (*e.g.* H_2-CoCat having onset deposition potential of –0.2 V vs. RHE)[34] could be expected on the ITO front-side and the steel back-side the solar cell, respectively. For other baths composed of both $[WS_4]^{2-}$ and Co^{2+}, the resultant devices showed η_{STH} performance in the range of 1.4-1.9% (**table 1**, entries 4, 6-8). The highest η_{STH} performance (1.9%) was achieved when the Co^{2+}/ $[WS_4]^{2-}$ molar ratio was exactly 1/2, corresponding to the stoichiometry of the $[Co(WS_4)_2]^{2-}$ precursor **(Figure S7)**. Hereafter, we focus on monolithic devices prepared under these optimized conditions.

We also measured the performances of the device in pH 0.3 (0.5 M H_2SO_4), 9.2 (borate buffer) and 14 (1M NaOH) electrolytes. While deterioration of the catalytic layers occurred within 20 min. of exposure to pH 0.3 and 14 electrolytes in the dark (**Figure S8**), the performance of the artificial leaf in pH9.2 borate buffer (**Figure S8**) was observed to be approximately half of that measured in neutral phosphate buffer. This lower performance could be the result of the instability of the CoWS catalyst, as previously shown for amorphous molybdenum sulfide.[35] For

this reason, we report in the following the data we measured in neutral phosphate electrolyte which has been also advocated by Costentin and Nocera for a safe and deployable technology.[36]

Table 1. Performance of resultant monolithic device in function of chemical deposition bath and catalyst deposition time employed for device assemblage

Entry	Catalyst deposition bath*			Performance of resultant monolithic device (η_{STH}, %)**
	Co^{2+} (mM)	$[WS_4]^{2-}$ (mM)	Catalyst photodeposition time (minutes)	
1	0.5	0.5	1	0.4
2	0.5	0.5	2	0.7
3	0.5	0.5	5	0.8
6	0.5	0.5	10	1.4
5	0.5	0.5	20	1.5
4	0.5	1.0	10	1.9
7	0.5	2.0	10	1.6
8	1.0	0.5	10	1.5
9	0.5	-	10	1.0
10	-	0.5	10	0

Note: (*) in pH 7 KPi 0.1M; (**) average solar-to-H_2 conversion yield calculated on the basis of 1h photocatalytic experiment

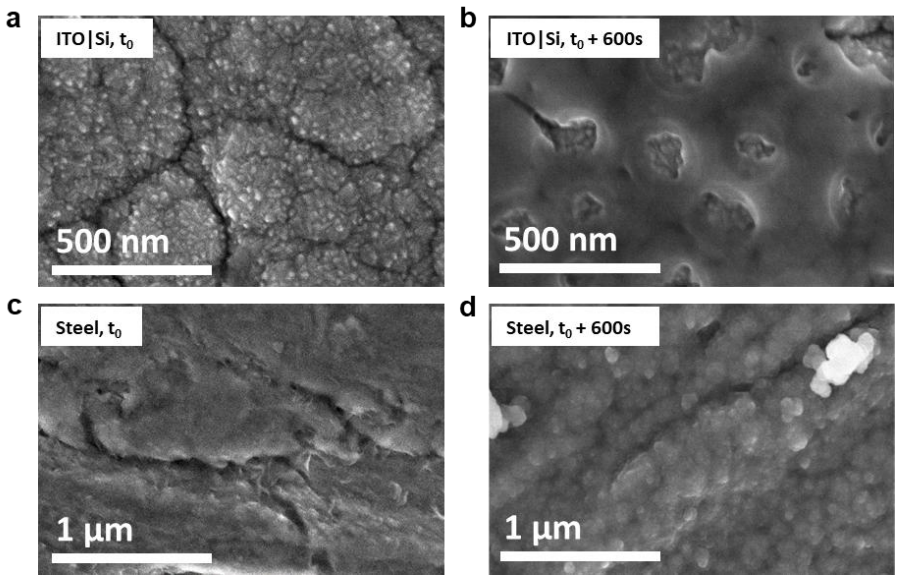

Figure 3. SEM images collected on the ITO front-side and Steel back-side of a pristine solar cell (**a,c**) and of a 1.9% device, namely after 10 minute of catalyst deposition (**b,d**)

Figure S9 shows digital photo taken on two sides of the 1.9% device when the preparation was completed. The ITO front-side changed from purple to blue-grey color whereas the Steel back-side changed from shining metal to dark brown color. We then performed a detail analysis on the morphology and chemical composition of the films grown on these surfaces. FE-SEM imaging showed a thin layer of CoWO which almost fully covered the ITO surface (**Figures 3a,b and S10**). No clear grain boundary could be distinguished. EDX analysis showed patterns of Co, W, O, P, Si and In elements. Si and In coming from the 3jn-a-Si and ITO layers, we inferred that the CoWO deposit was constituted of Co, W, O and P elements (**Figure S11**). The EDX elemental mapping revealed a homogeneous distribution of these elements over the whole CoWO layer **(Figure S12**). The chemical composition of the deposit was further characterized by XPS. In the W4f core spectrum, a doublet with $W4f_{7/2}$ binding energy of 35.36 eV was found, indicating the

presence of the W^{6+} oxidation state (**Figure S13**).[24, 37] In the Co2p spectrum, the main and satellite $Co2p_{3/2}$ were observed at 781.3 and 785.9 eV that suggested the presence of the Co^{2+} oxidation state.[25, 38] P 2p3/2 was found at 132.9 eV, being consistent with a phosphate species adsorbed onto cobalt oxide surface.[24, 34, 39-40] Sulfur was not found. Thus, all analysis performed on CoWO deposited onto ITO show full similarity with the same material deposited on FTO[24] and indicate that CoWO is an amorphous cobalt tungsten oxide having surface-bound phosphate species. **Figure S14** shows that, similarly to those deposited on FTO, the CoWO films deposited on ITO display a good stability when achieving continuous water oxidation in phosphate buffer. To gain more insights into the light absorption properties of this catalytic film, we fabricated CoWO films using electrodeposition on FTO substrates at 2 $mA.cm^{-2}$ current density corresponding to the value measured in wired configurations. CoWO films deposited on FTO are quite diffusive[41] and show a characteristic absorption peak at 380nm. To correct absorption measurements from light scattering, the absorbance at 550 nm, where CoWO films are fully transparent, was substracted from the absorbance measured at 380nm (**Figure S15**). In parallel, the thickness of the films was determined from SEM cross section images. Although with large data dispersion due to the inhomogeneityof the film over the whole sample as evidenced by color gradients in the CoWO films in **Figure S9, Figure S15** reveals a linear correlation of absorbance and film thickness with deposition time, allowing to determine a thickness of ~30 nm for films deposited over 10 min as in the optimized monolithic device.

On the steel surface, the CoWS deposit composed of small spherical nanoparticles with average size of 100 nm was observed (**Figure 3c,d, S16)**. The deposit was found compact and fully covering the steel surface. The EDX elemental mapping shows a homogeneous distribution of Co, W, O, P, and S elements over the deposit **(Figures S17, S18)**. XPS analysis showed Co2p,

W4f and P2p signatures similar to those recorded for the CoWO layer (**Figure S13**). A significant difference was the appearance of the S element, with two characteristic $S2p_{3/2}$ peaks[22] at 162.8 and 168.2 eV attributed to S^{2-} and a highly oxidized state like SO_4^{2-}, respectively. Thus, the CoWS deposit contains both surface-bound phosphate and surface species. It therefore resembles to the amorphous CoWS grown on a FTO electrode using the same $[Co(WS_4)_2]^{2-}$ deposition bath by applying a constant potential of –0.62V *vs.* Ag/AgCl.[22] **Figure S19** shows that, similarly to those deposited on FTO, the CoWS films deposited on steel display a good stability when achieving continuous H_2 evolution in phosphate buffer.

Evaluation of the performance of the monolithic device for overall solar water splitting

Figure 4a shows the actual evolution rates of H_2 and O_2 gases generated over illumination time using the optimized monolithic device in the pH 7 phosphate buffer solution. The molar H_2/O_2 ratio is 2:1, thus confirming the overall water splitting process. When the light illumination was stopped, e.g. after 3 hours of operation, the generation of H_2 and O_2 gases ended immediately and the accumulated amount of these gases remained constant (**figure 4b**). We thus conclude unambiguously that H_2 and O_2 were products of the overall solar water splitting process driven by the CoWO|ITO|3jn-a-Si|Steel|CoWS monolithic device. The average solar-to-hydrogen conversion yield (η_{STH}) of 1.9% was calculated based on 3 hour experiments. We note that the current performance is close to that reported by Nocera and coll. (η_{STH} of 2.5%) for a similar 3jn-a-Si solar cell loaded with CoPi OER and NiZnMo HER catalysts.[16] However, our current

device operates under more benign conditions, *e.g.* pH 7 phosphate buffer versus pH 9.2 borate buffer in the case of Nocera`s device.

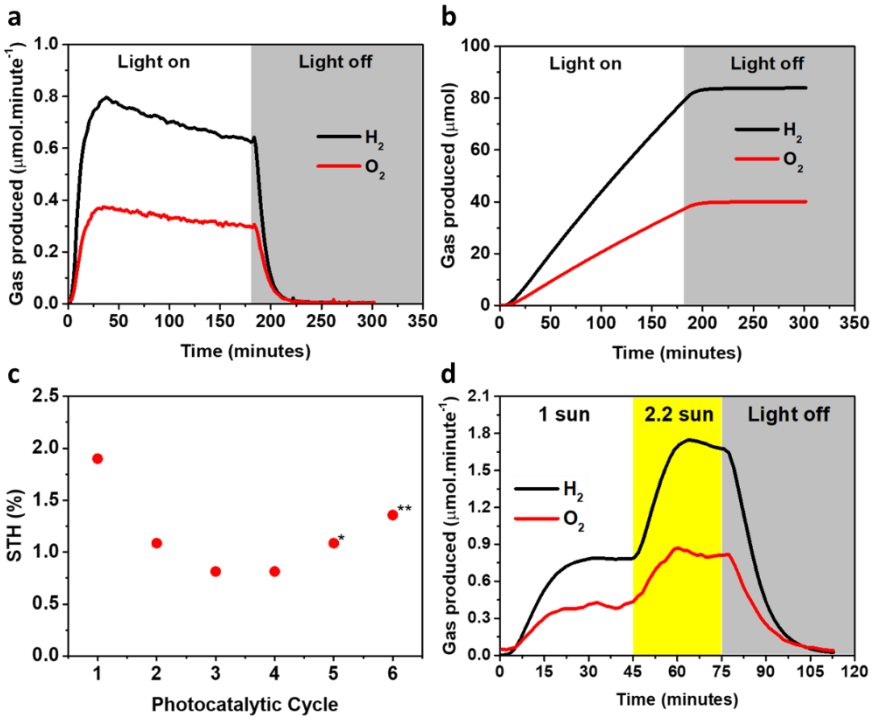

Figure 4. Assaying performance of an optimized monolithic device (η_{STH} = 1.9%) in a pH 7 KPi 0.1M solution. (**a**) Actual profiles of H_2 and O_2 produced gases recorded by an online gas chromatography, (**b**) Accumulated amount of these gases, (**c**) Average η_{STH} achieved over 3h when repeating the catalytic assay ((*) 0.025 mM and (**) 1.615 mM $(NH_4)_2[Co(WS_4)_2]$ was added in the 4th and 5th test cycle, respectively), (**d**) Actual profile of produced gases when varying the illumination intensity. Excepting in (**d**), illumination was made by the simulated 1 sun light.

The stability of the optimized monolithic device was then investigated in a series of solar water splitting experiment. Each experiment consisted of 3 hours light illumination. Between

experiments, the device was kept in the same solution in the dark for 72 hours. The device performance was found to decrease over time, reaching η_{STH} of ~0.8 % after 4 cycles, corresponding to 12 hours of operation in total (**Figures 4c and S20**). Adding $[Co(WS_4)_2]^{2-}$ to the operating phosphate medium allows to partly restore the device performance with η_{STH} of ~1.4 %. These result demonstrated the progressive degradation of the monolithic device but also its capability to heal with additional $[Co(WS_4)_2]^{2-}$catalyst precursor.

We finally examined the operation of this optimized monolithic device at higher irradiation power. To this end, the device was first conditioned under the standard simulated sunlight until the water splitting rate, quantified by an online gas chromatography, reached a steady value. Then, a Fresnel lens was used to concentrate the light illumination reaching the device to 2.2 sun. Immediately, the water splitting rate increased reaching a steady value 2.2 time higher than that obtained under 1 sun illumination (**Figure 4d**), thus with unmodified η_{STH} of 1.9%. This result indicates that the water splitting rate of the optimized monolithic device is still limited by the supply of photons to the the ITO|3jn-a-Si|Steel solar cell not by the catalytic ability of the CoWO-OER and CoWS-HER catalysts or the light harvester/catalysts interfacing.

Aforementioned, the device performance slightly decreased over the operation time, *e.g.* 18 % of the initial H_2 evolution rate was lost after 3 hours (**Figure 4a**). In order to gain insights into the performance degradation, we first characterized the catalyst layers after 3 hours of the catalytic operation. The CoWO layer showed no obvious change in surface morphology as revealed by FE-SEM analysis (**Figure S21**). Whereas, the CoWS layer experienced an obvious change in morphology. The spherical CoWS nanoparticles (~100 nm in diameter) transformed into wall-like objects suggesting a partial dissolution of the material during the H_2-evolving process (**Figure S22**). A similar structure conversion from amorphous structure to wall-like structure

under H_2-evolving conditions has been demonstrated in the case of molybdenum sulfide.[42-43] Unfortunately, attempts to compare the film thickness by a cross-section SEM analysis was not successful since the CoWO and CoWS films were too thin. In order to detect the catalyst partial dissolution, the chemical composition of the phosphate solution was analyzed using ICP-OES at different time intervals. Both dissolved Co and W were found, thus clearly confirming the partial dissolution of catalysts (**Figure S23**). However, for this monolithic device operation, it is not possible to easily distinguish the cathodic CoWS catalyst dissolution to the anodic CoWO catalyst dissolution, if the latter also occurs, nor to quantify the degree of redeposition of these catalysts. Indeed, efficient redeposition of cobalt, manganese and nickel oxides from low-concentration metal salts in electrolyte causing the healing capability of these catalysts has been previously reported.[44] However the situation experienced here is significantly more complex as we both deal with two distinct OER and HER catalysts and with bimetal catalysts with the possibility for monometallic phases to redeposit in addition to the initial bimetallic phases. The combination of these two phenomena prevented the modelling of the data shown in **Figure S23**.

Such dissolution/ redeposition processes likely alter the chemical composition of the CoWO and the CoWS layers over time, thus contributing to the decrease of performance of the monolithic device. This data is also consistent with the possibility to heal the deposits upon addition of $[Co(WS_4)_2]^{2-}$ in the electrolyte as discussed above (**Figures 4c and S20)**. To get more insights into these processes, it is however necessary to have additional information on the electrochemical potential at which they occur. This prompted us to develop methodologies allowing to monitor both the current density flowing through the device, as well as the electrochemical potential provided to the ITO and Steel electrodes by the 3jn-a-Si solar cell.

Investigation on operation of monolithic device: Half-cell assessment

In order to gain insights into the leaf operation, we first probed the operation of the two half-cells, namely the Steel│CoWS cathode and the CoWO│ITO│3jn-a-Si photoanode, in a pH 7 phosphate buffer electrolyte. The Steel│CoWS cathode was found to catalyze for the H_2 evolution with a moderate onset overpotential of 250 mV, being close to that recorded for a similar film deposited on FTO substrate (**figure 5a**).[22] To assay the CoWO│ITO│3jn-a-Si photoanode, an Ohmic contact was applied to the stainless steel base. Under the illumination of 1 sun light, the photoanode showed an onset photopotential of –0.66 V *vs.* RHE and a photocurrent density of ca. 9.0 mA.cm^{-2} at 1.23V vs. RHE applied potential (**figure 5b**, *red bold trace*).

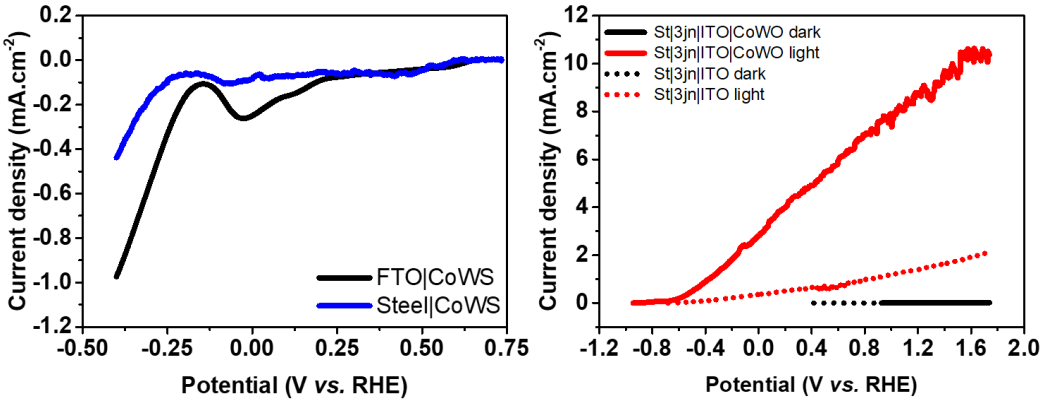

Figure 5. Current-voltage plot of a Steel│CoWS cathode (**left**) and a CoWO │ITO│3jn-a-Si photoanode (**right**) immersed in a pH 7 phosphate buffer. The photoanode was operated under 1 sun light illumination. Potential scan rate was 2 mV.s^{-1}.

Such performance proved superior to that previously reported for a CoPi | ITO | 3jn-a-Si photoanode operated in a pH 9.2 borate buffer (onset potential of –0.4 V *vs.* RHE and steady photocatalytic current of ca. 4 $mA.cm^{-2}$ at +0.55 V vs. RHE),[16] evidencing the advantage of the CoWO layer to promote catalytic O-evolution as compared to CoPi. A control measurement using a pristine ITO | 3jn-a-Si photoanode without decoration of a CoWO layer showed similar (–0.39 V vs RHE) onset photocurrent potential but significantly lower photocurrent density of less than 1.44 $mA.cm^{-2}$ at 1.23V *vs.* RHE (**figure 5b**, *red dotted trace*).

Investigation on operation of monolithic device: Operando analysis

Next, we designed an experiment aimed at probing the evolution of both the photovoltage and the photogenerated current circulating between the CoWO | ITO anode-side and the Steel | CoWS cathode-side of the monolithic device when it was illuminated. To this end, a biopotentiostat configuration was used. The CoWO-OER | ITO anode side of a monolithic device was interfaced with a pH 7 phosphate buffer electrolyte and exposed to light whereas its corresponding Steel | CoWS cathode side was exposed to air. To simulate this cathode, another Steel | CoWS electrode was fabricated by etching out the CoWO | ITO | 3jn-a-Si component from a monolithic device (*see the supporting information for more details*). The simulating Steel | CoWS cathode was immersed in the electrolyte but not exposed to light (**figure 6a**). The photoanode was used as a working electrode and the cathode as both counter and reference electrode. The potentiostat was then operated in chronoamperometric mode with an applied potential to the photoanode of 0 V vs the cathode. This reproduces the wired configuration already reported by Nocera and colleagues,[16] but allows monitoring the current flowing between both electrodes. Upon

illumination a photocurrent of ~2 mA.cm^{-2} was initially measured, in line with the recorded 1.9% STH efficiency of the system. This current density is however not stable with time and slowly decreases to 1-1.5 mA.cm^{-2} over a 3h period (**figure 6a**).

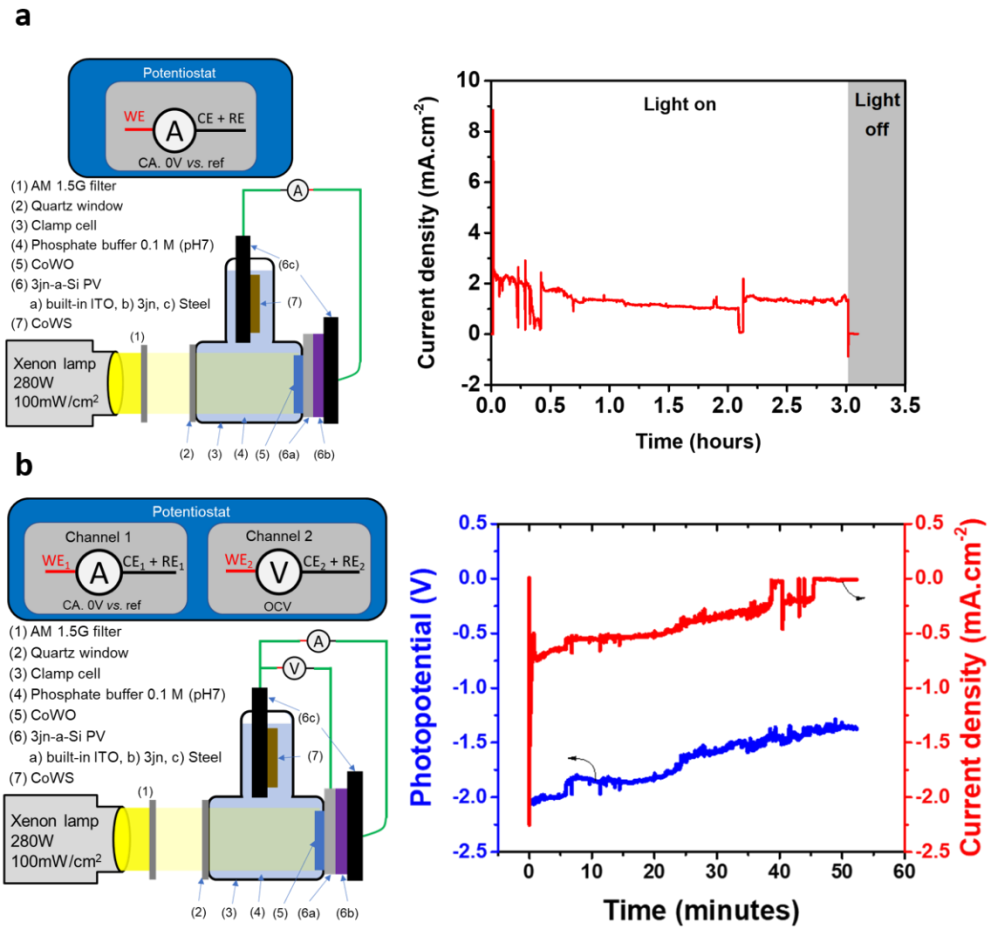

Figure 6. Schematic illustration of bipotentiostat configurations employed for evaluating the operation of a 1.9% monolithic device (left) and evolution of the photogenerated current over operation time (right) for a wired configuration without (**a**) and with (**b**) potential probing at the surface of the photoanode. The blue trace in Figure 6b shows the potential photogenerated by the 3jn-a-Si device.

In order to understand if this decrease of performance is due to a decrease of the photovoltage generated by the 3jn-a-Si cell, we then created an electrical contact on the top of the ITO layer. This contact was made using silver paste and was not immersed into the electrolyte (see the Supporting Information). A second channel of the potentiostat allowed monitoring the voltage between the ITO layer and the steel electrode in open-circuit potential mode (**figure 6b**). The photocurrent initially jumped to ~2 $mA.cm^{-2}$ as previously observed but then decays to 0.5 mA/cm^{-2} within a few seconds and continues to drop over the time of the experiment. The photovoltage, initially measured as expected from **Figure 1** at 2.05 V, continuously dropped during the experiment, which can explain the observed drop of current density as well (**figure 6b**). When repeating the bipotentiostat measurement for several devices, we obtained reproducible results with the same short life-time issue of the device. We assigned this discrepancy with regard to the stability observed over 12h for the whole cell to some detrimental side effect of the electrical connections made to monitor current and potential. This is heavily supported by the fact that, in this second monitoring mode, the current density is much lower than for the first one (**figure 6a**), suggesting that the contact on ITO generates defects that widely propagate through the whole layer and inactivates most of the device.

To identify the reasons for such a decrease in current density, we turned back to a fully wired configuration where the ITO front-side of the ITO│3jn-a-Si│Steel cell was wired to a fluorine-doped-tin-oxide (FTO) electrode while the steel back-side was wired to a Ag/AgCl reference electrode, both being immersed in a pH 7 phosphate buffer solution (*see **figure S24a** and the supporting information for experimental details).* This configuration indeed allows to measure potentials and currents to each electrode independently and simultaneously. An actual anodic

potential of 2.04 V *vs.* RHE and a cathodic potential of 0.10V vs RHE were recorded and found stable over 3 hours of measurement (**figure S24b**, red and black dash traces respectively). Thus, the photovoltage generated in this case was 1.94 V, quite similar to the value expected from **Figure 1**. Adding 0.5 mM $[Co(WS_4)_2]^{2-}$ into the phosphate electrolyte changed the chemical potential of the electrolyte that led to a shifting of the equilibrium at the FTO/electrolyte interface. As a result, it induced a shift of anodic potential to 1.58V and cathodic potential to –0.23V vs. RHE (**figure S24b**, red- and black-bold traces). The photovoltage recorded between two FTO electrodes in this case was 1.81V, representing a drop of 130 mV still sufficient to drive the deposition of CoWS and CoWO catalysts from the $[Co(WS_4)_2]^{2-}$ deposition bath. Indeed, under illumination, we observed a simultaneous growth of a dark brown CoWS layer and a CoWO layer on the surface of the two FTO electrodes. Bubbles simultaneously appeared on FTO electrodes that were identified to be O_2 and H_2 by gas chromatography. This confirms the simultaneous occurrence of both catalyst growth and overall water splitting.

After performing the photo-induced catalyst deposition for 10 minutes, the two electrodes were taken out from the $[Co(WS_4)_2]^{2-}$ deposition bath, intensively cleaned by DI water and immersed in a pH 7 phosphate buffer electrolyte and irradiated again with simulated sunlight. Here we used a tripotentiostat configuration to monitor both the photocurrent density flowing between the anode and the cathode and the electrochemical potentials of both the steel and ITO layers. Data are reported in **figure 7**. When the solar cell was illuminated by simulated sunlight, an anodic potential of 1.65V and a cathodic potential of –0.25V *vs.* RHE were recorded on the CoWO| ITO and Steel| CoWS electrode, respectively. These potentials were found to be stable over 24 hours (**figure 7b**, *purple and blue traces*). In total, the ITO | 3jn-a-Si | Steel solar cell generated a stable photovoltage of 1.9 V between the CoWO | ITO and Steel| CoWS electrodes, as for the

CoWO|ITO|3jn-a-Si|Steel|CoWS monolithic device (**figure 1).** This experiment allows to conclude that the contact with an aqueous electrolyte is the major cause for the degradation over time of the photopotential, and hence the photocurrent, of the CoWO|ITO|3jn-a-Si|Steel|CoWS artificial leaf.

The degradation of this fully wired device over several tens of min. was related to slow and limited corrosion of the catalysts in the HER/OER process (the photovoltage generated by the 3jn-a-Si cell remains constant). Accordingly, dissolved Co and W species were found in the phosphate electrolyte during the system operation as revealed by the ICP-OES analysis. Thus the accelerated degradation observed for the partially wired configuration (**figure 6b**) can be assigned to the degradation of the ITO|3jn-a-Si|Steel solar cell, causing a voltage drop and therefore a drop of the overall solar water splitting performance. In other words, the CoWO/ITO layer do not perfectly protect the inner 3jn-a-Si light harvesting component against corrosion. Actually, the oxidative corrosion of a native Si electrode could occur at an extremely low O_2 dissolved concentration, *e.g.* 15 ppb.[45] Thus, in the case a crack, a pin-hole or just a non-perfect coverage present on CoWO|ITO layer, the electrolyte-exposed Si layer would be quickly oxidized by the O_2 which evolves from nearby CoWO catalyst. We posit that the clamp configuration of the partially wired configuration we used can be responsible for the formation of such defects due to mechanical constrains, which in turns highlights the interest of the compact architecture of the monolithic artificial leaf. Still, this indicates that the deposition of a thicker ITO layer may be a solution to obtain more stable devices.

However, after an initial jump to ~2 $mA.cm^{-2}$, the photocurrent density generated in the separated photovoltaic-electrocatalytic, fully wired configuration rapidly decays to ~0.2 $mA.cm^{-2}$; It then appear to be quite stable with less than 10% decrease within 24 h (**figure 7b**). As

observed in the semi-wired configuration with potential sensing at the surface of the photoanode, the photocurrent is significantly lower than that of the full artificial leaf. This ten-fold lower value is in line with the solar-to-H_2 conversion yield η_{STH} of 0.23 % determined from the quantification of evolved H_2 gas, allowing to confirm a faradic efficiency of the water splitting catalysts close to 100% (**figure 7c**). Reasons for such an inactivation of ~90% of the device is still under investigation but may be related to the fabrication of an ohmic contact with the ITO layer.

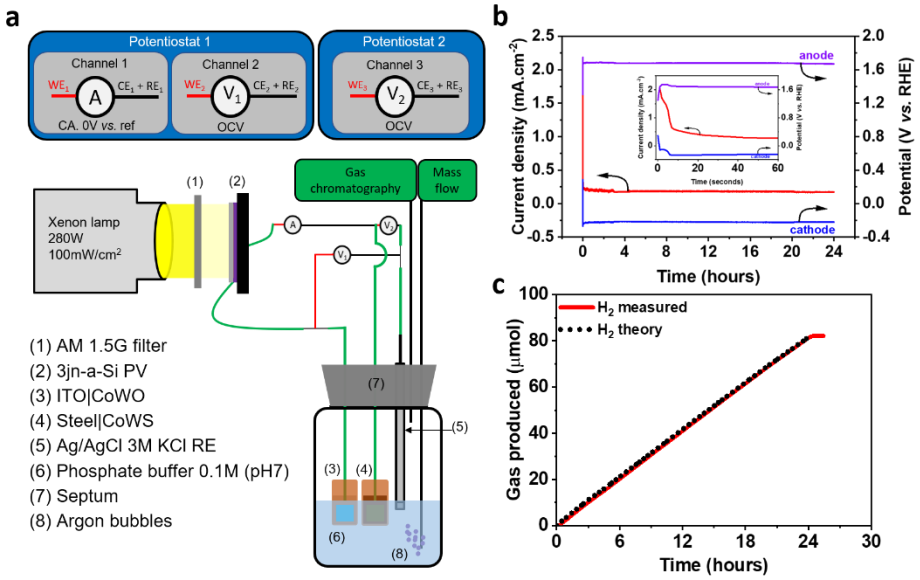

Figure 7. (a) Schematic illustration of tripotentiostate configuration employed to track anodic & cathodic potentials together with catalytic current flowing within the wired solar cell + electrolyser device under solar-induced operation; (**b**) Evolution of anodic potential, cathodic potential and catalytic current over time (the inset shows their evolution during the first minute); (**c**) Quantification of H_2 produced overtime. Electrolyte was a pH 7 KPi 0.1M solution. Illumination was provided by a simulated 1 sun light.

Conclusion

The development of the artificial leaf technology based on amorphous silicon triple junction solar cells requires the establishment of simple fabrication procedures. We report here on a novel method based on a simple $[Co(WS_4)_2]^{2-}$ electrolytic solution to simultaneously drive the photodeposition of O_2-evolving and H_2-evolving catalysts onto the respective anodic and cathodic sides of a triple junction Si solar cell. This rather simple solution process without a requirement of any high-tech facility allowed to create a complete CoWO |ITO| 3jn-a-Si| Steel| CoWS monolithic device for the overall solar water splitting application. The current best device offered a solar-to-H_2 conversion yield of 1.9% when being operated under benign conditions, *e.g.* in a pH 7 phosphate buffer solution, thus quite similar to previously reported performances. As observed for other hybrid PEC devices,[46-47] this STH yield is preserved when the irradiation intensity was increased, providing solutions for easy upscale of this technology with simple light management systems (e.g. mirrors and lenses) without increasing the amount of the expensive active material. The device performance slightly decreased over ~10 hours of operation time due to the partial dissolution of the catalysts that caused changes in their chemical composition and morphology. Such an aged device could recover most of its initial performance by adding the $[Co(WS_4)_2]^{2-}$ catalyst precursor into the phosphate operating condition. However, the main cause for long term degradation of the performances of the device are due to the instability of the silicon semi-conductor core due to exposure to the electrolyte, particularly enhanced by mechanical constrains or invasive modification of the ITO layer. Additional efforts should now focus on enforcing the electrochemical protection of this transparent catalyst/ITO layer.

ASSOCIATED CONTENT

Supporting Information. Experimental details, materials, methods and additional supporting figures and tables. The supplementary information is available free of charge via the Internet at http://pubs.acs.org.

AUTHOR INFORMATION

Corresponding Authors

* Dr. Vincent Artero; vincent.artero@cea.fr ;

* Dr. Phong D Tran; tran-dinh.phong@usth.edu.vn

Notes

The authors declare no conflict of interests.

ACKNOWLEDGEMENTS

This work was supported by the National Foundation for Science and Technology Development (NAFOSTED, project 103.99-2019.328) and the Agence Nationale de la Recherche (Labex ARCANE, CBH-EUR-GS, ANR-17-EURE-0003). Duc N. Nguyen thanks the French Embassy in Hanoi for an excellence grant. We thank Dr. Truong Quang Duc from Tohoku University (Japan) for XPS measurement support.

REFERENCES AND NOTES

1. Rongé, J.; Bosserez, T.; Martel, D.; Nervi, C.; Boarino, L.; Taulelle, F.; Decher, G.; Bordiga, S.; Martens, J. A., Monolithic cells for solar fuels. *Chem. Soc. Rev.* **2014,** *43*, 7963-7981.
2. Tembhurne, S.; Nandjou, F.; Haussener, S., A thermally synergistic photo-electrochemical hydrogen generator operating under concentrated solar irradiation. *Nat. Energy* **2019,** *4*, 399-407.
3. Cheng, W.-H.; de la Calle, A.; Atwater, H. A.; Stechel, E. B.; Xiang, C., Hydrogen from Sunlight and Water: A Side-by-Side Comparison between Photoelectrochemical and Solar Thermochemical Water-Splitting. *ACS Energy Lett.* **2021,** *6*, 3096-3113.
4. Kim, H.; Bae, S.; Jeon, D.; Ryu, J., Fully solution-processable Cu_2O–$BiVO_4$ photoelectrochemical cells for bias-free solar water splitting. *Green Chem.* **2018,** *20*, 3732-3742.
5. Wang, Q.; Hisatomi, T.; Jia, Q.; Tokudome, H.; Zhong, M.; Wang, C.; Pan, Z.; Takata, T.; Nakabayashi, M.; Shibata, N.; Li, Y.; Sharp, I. D.; Kudo, A.; Yamada, T.; Domen, K., Scalable water splitting on particulate photocatalyst sheets with a solar-to-hydrogen energy conversion efficiency exceeding 1%. *Nat. Mater.* **2016,** *15*, 611-615.

6. Goto, Y.; Hisatomi, T.; Wang, Q.; Higashi, T.; Ishikiriyama, K.; Maeda, T.; Sakata, Y.; Okunaka, S.; Tokudome, H.; Katayama, M.; Akiyama, S.; Nishiyama, H.; Inoue, Y.; Takewaki, T.; Setoyama, T.; Minegishi, T.; Takata, T.; Yamada, T.; Domen, K., A Particulate Photocatalyst Water-Splitting Panel for Large-Scale Solar Hydrogen Generation. *Joule* **2018,** *2*, 509-520.
7. Nishiyama, H.; Yamada, T.; Nakabayashi, M.; Maehara, Y.; Yamaguchi, M.; Kuromiya, Y.; Nagatsuma, Y.; Tokudome, H.; Akiyama, S.; Watanabe, T.; Narushima, R.; Okunaka, S.; Shibata, N.; Takata, T.; Hisatomi, T.; Domen, K., Photocatalytic solar hydrogen production from water on a 100 m^2 scale. *Nature* **2021,** *598*, 304-307.
8. Windle, C. D.; Kumagai, H.; Higashi, M.; Brisse, R.; Bold, S.; Jousselme, B.; Chavarot-Kerlidou, M.; Maeda, K.; Abe, R.; Ishitani, O.; Artero, V., Earth-Abundant Molecular Z-Scheme Photoelectrochemical Cell for Overall Water-Splitting. *J. Am. Chem. Soc.* **2019,** *141*, 9593-9602.
9. Sherman, B. D.; Sheridan, M. V.; Wee, K.-R.; Marquard, S. L.; Wang, D.; Alibabaei, L.; Ashford, D. L.; Meyer, T. J., A Dye-Sensitized Photoelectrochemical Tandem Cell for Light Driven Hydrogen Production from Water. *J. Am. Chem. Soc.* **2016,** *138*, 16745-16753.
10. Luo, J.; Im, J.-H.; Mayer, M. T.; Schreier, M.; Nazeeruddin, M. K.; Park, N.-G.; Tilley, S. D.; Fan, H. J.; Grätzel, M., Water photolysis at 12.3% efficiency via perovskite photovoltaics and Earth-abundant catalysts. *Science* **2014,** *345*, 1593-1596.
11. Gao, J.; Sahli, F.; Liu, C.; Ren, D.; Guo, X.; Werner, J.; Jeangros, Q.; Zakeeruddin, S. M.; Ballif, C.; Grätzel, M.; Luo, J., Solar Water Splitting with Perovskite/Silicon Tandem Cell and TiC-Supported Pt Nanocluster Electrocatalyst. *Joule* **2019,** *3*, 2930-2941.
12. Lin, R.; Lei, H.; Ruan, D.; Jiang, K.; Yu, X.; Wang, Z.; Mai, W.; Yan, H., Solar-powered overall water splitting system combing metal-organic frameworks derived bimetallic nanohybrids based electrocatalysts and one organic solar cell. *Nano Energy* **2019,** *56*, 82-91.
13. Schüttauf, J.-W.; Modestino, M. A.; Chinello, E.; Lambelet, D.; Delfino, A.; Dominé, D.; Faes, A.; Despeisse, M.; Bailat, J.; Psaltis, D.; Moser, C.; Ballif, C., Solar-to-Hydrogen Production at 14.2% Efficiency with Silicon Photovoltaics and Earth-Abundant Electrocatalysts. *J. Electrochem. Soc.* **2016,** *163*, F1177-F1181.
14. Eftekharinia, B.; Pezeshki, H.; Dabirian, A., Unassisted Water Splitting Using Standard Silicon Solar Cells Stabilized with Copper and Bifunctional NiFe Electrocatalysts. *ACS Appl. Mater. Interfaces* **2020,** *12*, 17424-17435.
15. Rocheleau, R. E.; Miller, E. L.; Misra, A., High-Efficiency Photoelectrochemical Hydrogen Production Using Multijunction Amorphous Silicon Photoelectrodes. *Energy Fuels* **1998,** *12*, 3-10.
16. Reece, S. Y.; Hamel, J. A.; Sung, K.; Jarvi, T. D.; Esswein, A. J.; Pijpers, J. J. H.; Nocera, D. G., Wireless Solar Water Splitting Using Silicon-Based Semiconductors and Earth-Abundant Catalysts. *Science* **2011,** *334*, 645-648.
17. Surendranath, Y.; Bediako, D. K.; Nocera, D. G., Interplay of oxygen-evolution kinetics and photovoltaic power curves on the construction of artificial leaves. *Proc. Natl. Acad. Sci. USA* **2012,** *109*, 15617-15621.
18. Cox, C. R.; Lee, J. Z.; Nocera, D. G.; Buonassisi, T., Ten-percent solar-to-fuel conversion with nonprecious materials. *Proc. Natl. Acad. Sci. USA* **2014,** *111*, 14057-14061.
19. Merki, D.; Vrubel, H.; Rovelli, L.; Fierro, S.; Hu, X., Fe, Co, and Ni ions promote the catalytic activity of amorphous molybdenum sulfide films for hydrogen evolution. *Chem. Sci.* **2012,** *3*, 2515-2525.
20. Chen, Y.; Tran, P. D.; Boix, P.; Ren, Y.; Chiam, S. Y.; Li, Z.; Fu, K.; Wong, L. H.; Barber, J., Silicon Decorated with Amorphous Cobalt Molybdenum Sulfide Catalyst as an Efficient Photocathode for Solar Hydrogen Generation. *ACS Nano* **2015,** *9*, 3829-3836.
21. Karikalan, N.; Sundaresan, P.; Chen, S.-M.; Karthik, R.; Karuppiah, C., Cobalt molybdenum sulfide decorated with highly conductive sulfur-doped carbon as an electrocatalyst for the enhanced activity of hydrogen evolution reaction. *Int. J. Hydrogen Energy* **2019,** *44*, 9164-9173.

22. Tran, P. D.; Chiam, S. Y.; Boix, P. P.; Ren, Y.; Pramana, S. S.; Fize, J.; Artero, V.; Barber, J., Novel cobalt/nickel–tungsten-sulfide catalysts for electrocatalytic hydrogen generation from water. *Energy Environ. Sci.* **2013,** *6*, 2452-2459.
23. Yang, L.; Wu, X.; Zhu, X.; He, C.; Meng, M.; Gan, Z.; Chu, P. K., Amorphous nickel/cobalt tungsten sulfide electrocatalysts for high-efficiency hydrogen evolution reaction. *Appl. Surf. Sci.* **2015,** *341*, 149-156.
24. Nguyen, L. N.; Thuy, U. T. D.; Truong, Q. D.; Honma, I.; Nguyen, Q. L.; Tran, P. D., Electrodeposited Amorphous Tungsten-doped Cobalt Oxide as an Efficient Catalyst for the Oxygen Evolution Reaction. *Chemistry – An Asian Journal* **2018,** *13*, 1530-1534.
25. Zhao, Y.; Wang, Y.; Dong, Y.; Carlos, C.; Li, J.; Zhang, Z.; Li, T.; Shao, Y.; Yan, S.; Gu, L.; Wang, J.; Wang, X., Quasi-Two-Dimensional Earth-Abundant Bimetallic Electrocatalysts for Oxygen Evolution Reactions. *ACS Energy Lett.* **2021**, 3367-3375.
26. Nakayama, M.; Takeda, A.; Maruyama, H.; Kumbhar, V.; Crosnier, O., Cobalt-substituted iron-based wolframite synthesized via polyol route for efficient oxygen evolution reaction. *Electrochem. Commun.* **2020,** *120*, 106834.
27. Kumaravel, S.; Thiruvengetam, P.; Ede, S. R.; Karthick, K.; Anantharaj, S.; Sam Sankar, S.; Kundu, S., Cobalt tungsten oxide hydroxide hydrate (CTOHH) on DNA scaffold: an excellent bi-functional catalyst for oxygen evolution reaction (OER) and aromatic alcohol oxidation. *Dalton Trans.* **2019,** *48*, 17117-17131.
28. Yadav, A. A.; Hunge, Y. M.; Kang, S.-W., Highly efficient porous morphology of cobalt molybdenum sulfide for overall water splitting reaction. *Surfaces and Interfaces* **2021,** *23*, 101020.
29. Ray, C.; Lee, S. C.; Sankar, K. V.; Jin, B.; Lee, J.; Park, J. H.; Jun, S. C., Amorphous Phosphorus-Incorporated Cobalt Molybdenum Sulfide on Carbon Cloth: An Efficient and Stable Electrocatalyst for Enhanced Overall Water Splitting over Entire pH Values. *ACS Appl. Mater. Interfaces* **2017,** *9*, 37739-37749.
30. Xunming, D. In *Optimization of a-SiGe based triple, tandem and single-junction solar cells*, Conference Record of the Thirty-first IEEE Photovoltaic Specialists Conference, 2005., 3-7 Jan. 2005; 2005; pp 1365-1370.
31. Bhanawat, A.; Zhu, K.; Pilon, L., How do bubbles affect light absorption in photoelectrodes for solar water splitting? *Sustainable Energy & Fuels* **2022,** *6*, 910-924.
32. Müller, A.; Jostes, R.; Flemming, V.; Potthast, R., Delocalized molecular orbitals in the trimetallic thioheteroanion $[S_2WS_2CoS_2SW_2]^{2-}$: spectroscopic and cyclic voltammetric results. *Inorg. Chim. Acta* **1980,** *44*, L33-L35.
33. Kanan, M. W.; Nocera, D. G., In Situ Formation of an Oxygen-Evolving Catalyst in Neutral Water Containing Phosphate and Co^{2+}. *Science* **2008,** *321*, 1072-1075.
34. Cobo, S.; Heidkamp, J.; Jacques, P.-A.; Fize, J.; Fourmond, V.; Guetaz, L.; Jousselme, B.; Ivanova, V.; Dau, H.; Palacin, S.; Fontecave, M.; Artero, V., A Janus cobalt-based catalytic material for electro-splitting of water. *Nat. Mater.* **2012,** *11*, 802-807.
35. Tran, P. D.; Tran, T. V.; Orio, M.; Torelli, S.; Truong, Q. D.; Nayuki, K.; Sasaki, Y.; Chiam, S. Y.; Yi, R.; Honma, I.; Barber, J.; Artero, V., Coordination polymer structure and revisited hydrogen evolution catalytic mechanism for amorphous molybdenum sulfide. *Nat. Mater.* **2016,** *15*, 640-646.
36. Costentin, C.; Nocera, D. G., Self-healing catalysis in water. *Proc. Natl. Acad. Sci. USA* **2017,** *114*, 13380-13384.
37. Chakrabarti, S.; Samanta, S.; Maikap, S.; Rahaman, S. Z.; Cheng, H.-M., Temperature-Dependent Non-linear Resistive Switching Characteristics and Mechanism Using a New $W/WO_3/WO_x/W$ Structure. *Nanoscale Research Letters* **2016,** *11*, 389.

38. Zang, M.; Xu, N.; Cao, G.; Chen, Z.; Cui, J.; Gan, L.; Dai, H.; Yang, X.; Wang, P., Cobalt Molybdenum Oxide Derived High-Performance Electrocatalyst for the Hydrogen Evolution Reaction. *ACS Catal.* **2018,** *8*, 5062-5069.
39. Laudadio, E. D.; Bennett, J. W.; Green, C. M.; Mason, S. E.; Hamers, R. J., Impact of Phosphate Adsorption on Complex Cobalt Oxide Nanoparticle Dispersibility in Aqueous Media. *Environ.Sci. Technol.* **2018,** *52*, 10186-10195.
40. Di Palma, V.; Zafeiropoulos, G.; Goldsweer, T.; Kessels, W. M. M.; van de Sanden, M. C. M.; Creatore, M.; Tsampas, M. N., Atomic layer deposition of cobalt phosphate thin films for the oxygen evolution reaction. *Electrochem. Commun.* **2019,** *98*, 73-77.
41. We preferred FTO to ITO substrates as they allow increased reproducibility of the measures in terms of scattering.
42. Lee, S. C.; Benck, J. D.; Tsai, C.; Park, J.; Koh, A. L.; Abild-Pedersen, F.; Jaramillo, T. F.; Sinclair, R., Chemical and Phase Evolution of Amorphous Molybdenum Sulfide Catalysts for Electrochemical Hydrogen Production. *ACS Nano* **2016,** *10*, 624-632.
43. Xi, F.; Bogdanoff, P.; Harbauer, K.; Plate, P.; Höhn, C.; Rappich, J.; Wang, B.; Han, X.; van de Krol, R.; Fiechter, S., Structural Transformation Identification of Sputtered Amorphous MoS_x as an Efficient Hydrogen-Evolving Catalyst during Electrochemical Activation. *ACS Catal.* **2019,** *9*, 2368-2380.
44. Thorarinsdottir, A. E.; Veroneau, S. S.; Nocera, D. G., Self-healing oxygen evolution catalysts. *Nat. Commun.* **2022,** *13*, 1243.
45. Hou, Y.; Abrams, B. L.; Vesborg, P. C. K.; Björketun, M. E.; Herbst, K.; Bech, L.; Setti, A. M.; Damsgaard, C. D.; Pedersen, T.; Hansen, O.; Rossmeisl, J.; Dahl, S.; Nørskov, J. K.; Chorkendorff, I., Bioinspired molecular co-catalysts bonded to a silicon photocathode for solar hydrogen evolution. *Nat. Mater.* **2011,** *10*, 434-438.
46. Wadsworth, B. L.; Beiler, A. M.; Khusnutdinova, D.; Reyes Cruz, E. A.; Moore, G. F., Interplay between Light Flux, Quantum Efficiency, and Turnover Frequency in Molecular-Modified Photoelectrosynthetic Assemblies. *J. Am. Chem. Soc.* **2019,** *141*, 15932-15941.
47. Nishiori, D.; Wadsworth, B. L.; Moore, G. F., Parallels between enzyme catalysis, electrocatalysis, and photoelectrosynthesis. *Chem Catalysis* **2021,** *1*, 978-996.